Cell, Vol. 71, 107–118, October 2, 1992, Copyright © 1992 by Cell Press

The Structure of Human Mitochondrial Manganese Superoxide Dismutase Reveals a Novel Tetrameric Interface of Two 4-Helix Bundles

Gloria E. O. Borgstahl,* Hans E. Parge,* Michael J. Hickey,* Wayne F. Beyer, Jr.,† Robert A. Hallewell,* and John A. Tainer*
*Department of Molecular Biology
The Scripps Research Institute
La Jolla, California 92037
†Department of Biochemistry
Duke University Medical Center
Durham, North Carolina 27710

Summary

The 2.2 Å resolution crystal structure of recombinant human manganese superoxide dismutase, a homotetrameric enzyme that protects mitochondria against oxygen-mediated free radical damage, has been determined. Within each subunit, both the N-terminal helical hairpin and C-terminal α/β domains contribute ligands to the catalytic manganese site. Two identical 4-helix bundles, symmetrically assembled from the N-terminal helical hairpins, form novel tetrameric interfaces that stabilize the active sites. Structurally altered polymorphic variants with reduced activity, such as tetrameric interface mutant Ile-58 to Thr, may produce not only an early selective advantage, through enhanced cytotoxicity of tumor necrosis factor for virus-infected cells, but also detrimental effects from increased mitochondrial oxidative damage, contributing to degenerative conditions, including diabetes, aging, and Parkinson's and Alzheimer's diseases.

Introduction

Mitochondria consume over 90% of the cell's oxygen, and the mitochondrial respiratory chain is the source of a large flux of oxygen radicals (Chance et al., 1979). Mitochondrial DNA is especially subject to oxidative damage due to this immense oxygen metabolism, relatively inefficient DNA repair, and lack of histones (Richter et al., 1988). Within mitochondria, manganese superoxide dismutase (MnSOD) is of biological interest as a primary defense against oxidative damage (Beyer et al., 1991). MnSOD thus represents a major class of the SOD metalloenzymes, which all act to dismute toxic superoxide radicals to oxygen and hydrogen peroxide.

Superoxide is a normal byproduct of aerobic metabolism and is produced in many reactions, including oxidative phosphorylation, photosynthesis, and the respiratory burst of stimulated neutrophils and macrophages (Fridovich, 1986; Halliwell and Gutteridge, 1989). Damage inflicted by active oxygen species has been implicated in many degenerative processes, including cancer and aging (Ames, 1983; Cerutti, 1985; Floyd, 1991; Fraga et al., 1990; Harman, 1981). The rate of oxidative DNA damage has been shown to be directly related to the metabolic rate and inversely related to life span (Adelman et al., 1988).

SODs are critical components in the physiological response to oxygen toxicity and are actively investigated as potential therapeutic agents in pathological conditions related to oxidative stress, e.g., postischemic reperfusion of organs (Murohara et al., 1991; Zweier et al., 1987), lung and tissue damage (White et al., 1991; Oda et al., 1989), acute and chronic inflammation, and ionizing radiation (Halliwell et al., 1985). Recent experiments support antiaging and anticancer roles for SODs (Halliwell and Gutteridge, 1989). Increased SOD expression in Drosophila results in a small but significant increase in mean life span (Reveillaud et al., 1991). The level of SOD induced in human leukocytes by paraquat decreases with age, but increased levels of induction are correlated with longevity (Niwa et al., 1990). SODs are also involved in the pervasive bioregulatory functions of nitric oxide by preventing nitric oxide peroxidation by superoxide (Nakazono et al., 1991).

Three forms of SOD with different catalytic metal ions have distinct distributions (Beyer et al., 1991). Cu,ZnSOD occurs primarily in eukaryotes, but has also been found in bacterial pathogens. FeSOD is found in prokaryotes, and MnSOD is found in both prokaryotes and mitochondria. Fe and MnSODs share a similar α/β fold (Stallings et al., 1984) and are structurally unrelated to the Greek key β-barrel fold of Cu,ZnSOD (Tainer et al., 1982).

In vivo, Cu,ZnSOD and FeSOD are constitutively produced, but MnSOD is inducible (Hassan, 1988; Touati, 1988). Induction of MnSOD has been observed following treatment with paraquat (Krall et al., 1988), X-radiation (Oberley et al., 1987), hyperoxia (Housset and Junod, 1981), interleukin-1 (Masuda et al., 1988), and tumor necrosis factor (Wong et al., 1989). Thus increased levels of MnSOD provide protection during periods of oxidative stress. For medical uses, MnSOD may have unique advantages. Unlike the FeSOD and Cu,ZnSOD enzymes, MnSOD does not exhibit product inhibition by hydrogen peroxide (Beyer and Fridovich, 1987). Also, MnSOD has a half-life in sera of 5–6 hr compared with 6–10 min for the Cu,ZnSOD (Gorecki et al., 1991).

The relatively long serum half-life of human MnSOD is apparently due to its assembly (Gorecki et al., 1991), suggesting the importance of its tetrameric interactions. In fact, the various SODs are distinguished according to their modes of subunit aggregation (Tainer et al., 1991). The intracellular Cu,ZnSODs are invariably dimeric. Most FeSODs are dimers, with the exception of a tetrameric FeSOD isolated from Methanobacterium bryantii (Kirby et al., 1981). Eukaryotic MnSODs are usually tetrameric, while the prokaryotic enzymes are usually dimeric. Exceptions are the tetrameric MnSODs from the extreme thermophiles Thermus thermophilus (Sato and Nakasawa, 1978) and Thermus aquaticus (Sato and Harris, 1977).

Despite the biological importance of mitochondrial MnSOD, no crystallographic structure has been available. Establishing the three-dimensional structure of any macromolecule that has potential for human drug use is advantageous. The Cu,ZnSOD structure has allowed the design

of mutant enzymes that are more thermostable (Parge et al., 1992; McRee et al., 1990), have a longer serum half-life (Hallewell et al., 1989), and are more active (Getzoff et al., 1992), demonstrating the utility of structural information for protein design. Here, we present the structure of human MnSOD at 2.2 Å resolution, highlighting the roles of specific structural elements and side chain interactions in controlling the enzyme's stability and assembly. These results implicate a polymorphic variation of the major tetramer interface residue Ile-58 in defective MnSOD assembly and activity and potentially in increased mitochondrial oxidative damage contributing to autoimmune and degenerative diseases. This structure should aid future biochemical, mutagenic, and biological studies aimed at understanding the enzyme's biological function at the atomic level.

Results and Discussion

Structure Determination and Quality

Based upon the atomic structure of the human mitochondrial MnSOD tetramer determined at 2.2 Å resolution with an R factor of 17.1% (see Experimental Procedures), the 198 residues of each subunit fold into three strands of antiparallel β sheet, seven α helices, seven connecting structures (named A through J), and the N- and C-termini (Figure 1A). The excellent main-chain geometry and overall secondary structure composition are shown in a Ramachandran plot of the ϕ,ψ angles (Figure 1B). The two subunits of the crystallographic asymmetric unit pack tightly together to resemble structurally bacterial SOD dimers (Beyer et al., 1991), with both subunits participating in the formation of the two active sites (Figure 2). The two subunits are very similar in structure, as indicated by superposition of the main-chain atoms of regular secondary structural elements (root mean square deviation, 0.30 Å), of all main-chain atoms (0.33 Å), and of all atoms (0.93 Å, higher value because of side chain variation due to crystal lattice contacts).

Subunit Fold and Active Site Geometry

The subunit fold has dimensions of about 40 × 47 × 49 Å and can be divided into two distinct domains: an N-terminal helical hairpin domain and a C-terminal α/β domain, containing a three-stranded antiparallel β sheet and five α helices (Figure 3A).

The N-terminal domain is composed of residues 1–84 and is formed primarily by two long antiparallel α helices separated by a tight turn, forming a helical hairpin structure. Residues 1–10 have an extended structure and are packed against helices α1 and α2. Residue Pro-16 is a cis Pro in position three of a type VIa turn. The first long helix, α1, extends from Ala-20 through Ala-50 and is bent at Ser-28. Helix α2 extends from Val-54 to Asn-80 and is bent at Pro-62. The bends in the helices give a left-handed twist to the hairpin. The C-terminus of helix α2 tightens, and the last 4 residues form 3_{10} hydrogen bonds. Helices α1 and α2 are joined by a type I tight turn, forming a helical hairpin

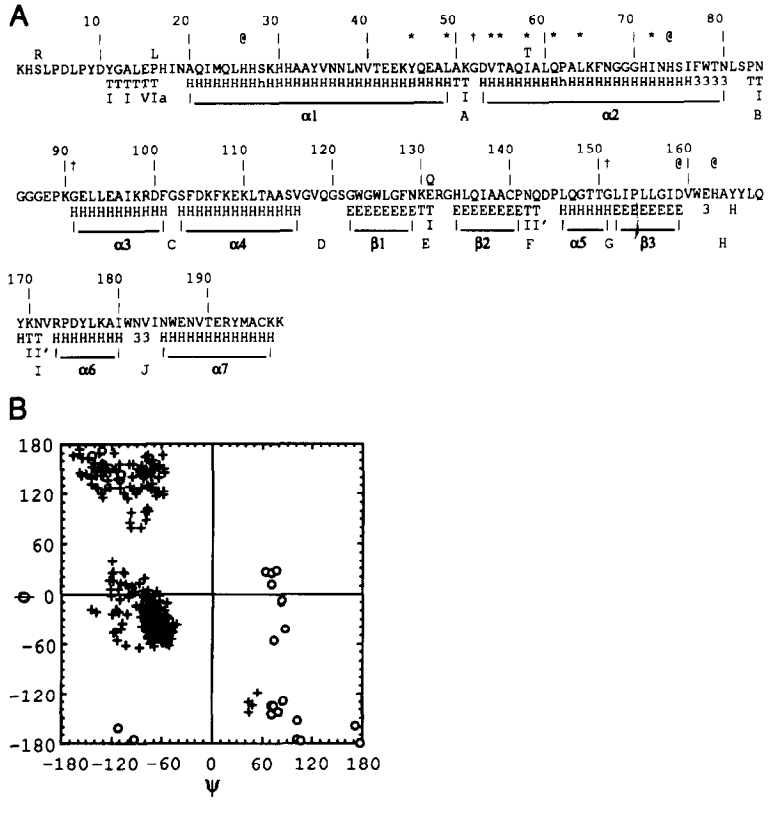

Figure 1. Conformation of the Human Mitochondrial MnSOD Subunit

(A) Secondary structure assignment of the 198 residue human MnSOD subunit. The amino acid sequence numbers are on line 1. On line 2, @ marks the metal ligands, an asterisk indicates the 8 residues that contribute the most buried surface area to the 4-helix bundle interface, and † marks the position of the exon boundaries of the rat MnSOD gene (Ho et al., 1991). Line 3 indicates the positions of sequence polymorphisms, and line 4 indicates the sequence of normal human MnSOD in one-letter code (Beck et al., 1987; Ho and Crapo, 1988; Church, 1990; St. Clair and Holland, 1991; Wispe et al., 1989; Heckl, 1988). Secondary structure assignments are coded on line 5: H, α helix (n + 4 main-chain hydrogen bonding); h, bend in α helix (one main-chain hydrogen bond broken); 3, 3_{10} helix (n + 3 main-chain hydrogen bonding); E, β strand; T, residues 2 and 3 of a tight turn. Line 6 shows the boundaries of the major helices (α1–α7), β strands (β1–β3), and the positions of type I, type II', and type VIa tight turns and other connecting structures (labeled A–J). (B) A Ramachandran diagram (Ramachandran and Sasisekharan, 1968) of the ϕ,ψ main-chain dihedral angles for A and B subunits (one crystallographic asymmetric unit). Gly residues are indicated by open circles and nonglycine residues by plus signs. All values lie in allowed regions. Residues Asn-142 and Lys-170 have values in the lower right quadrant and are at the second position of type II' turns.

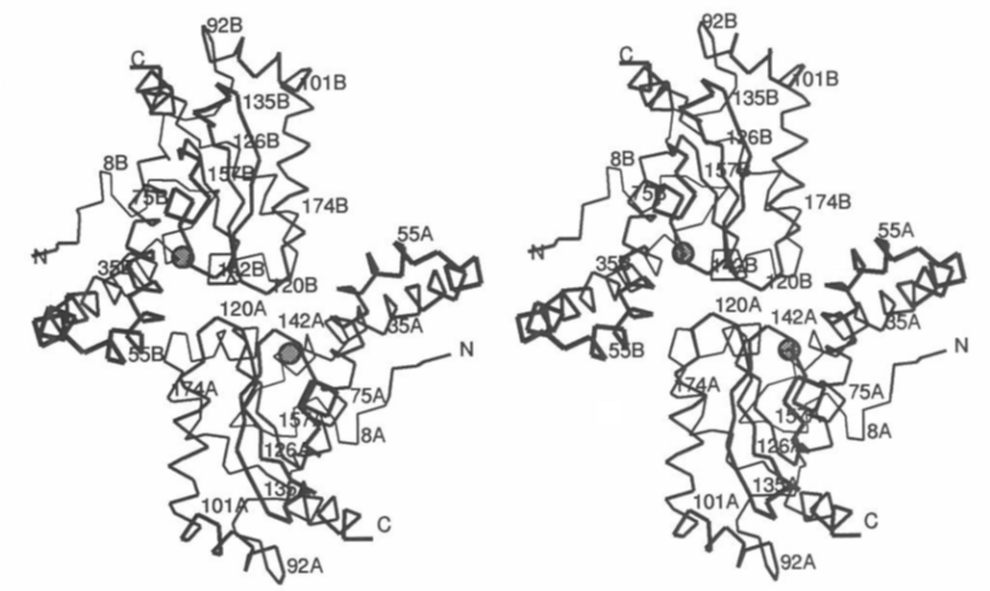

Figure 2. C^{α} Trace of the Two Subunits That Form the Crystallographic Asymmetric Unit and the Dimer Interface

Stereo diagram of the C^{α} trace of the A and B subunits, viewed down the noncrystallographic 2-fold symmetry axis. C^{α} positions are periodically identified by residue number and subunit letter where space permits. The complete tetramer is generated from this crystallographic asymmetric unit by a 2-fold rotation about the crystallographic c axis, which is horizontal in this view. The dimeric asymmetric unit of the MnSOD tetramer is structurally similar to the Fe and MnSOD bacterial dimeric enzymes. The manganese ions (shaded spheres) are close to the dimer interface. The A and B subunits are intimately associated, with residues Glu-162 and Tyr-166 from one subunit contributing to the active site of the neighboring subunit.

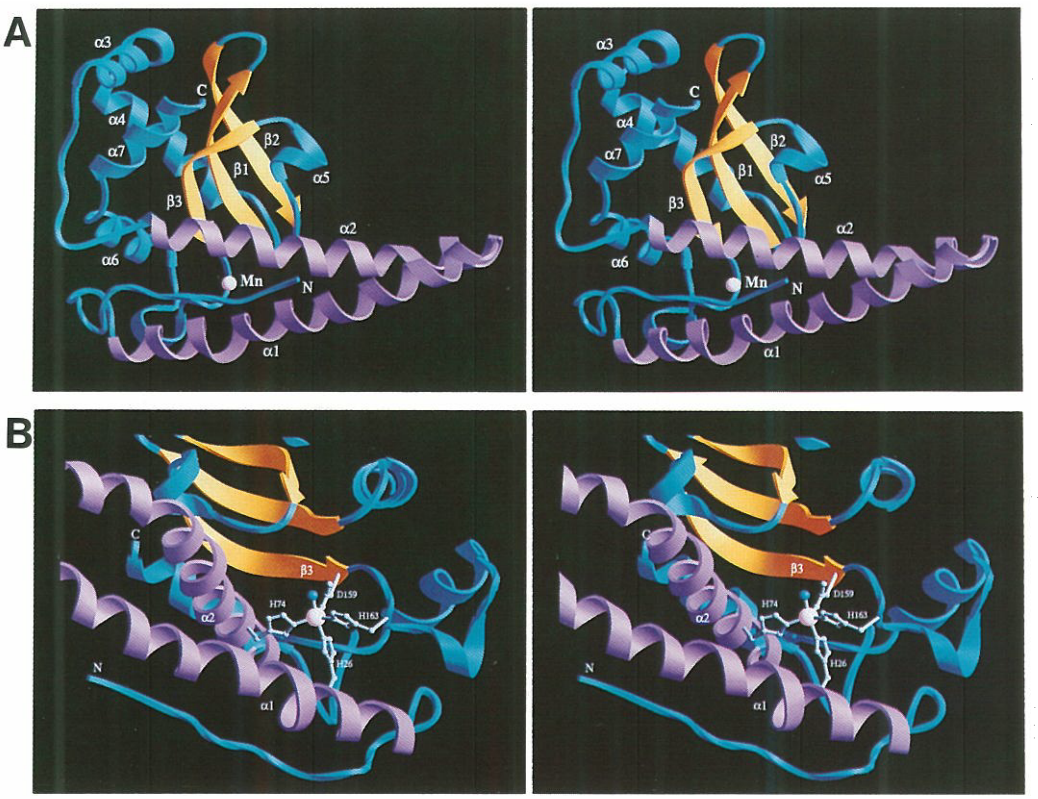

Figure 3. Human Mitochondrial MnSOD Subunit Fold and Active Site Geometry

Stereo RIBBONS diagrams (Carson, 1991) of human MnSOD subunit fold. Manganese ions are shown as light pink spheres. Secondary structure definitions are as designated in Figure 1A. (A) MnSOD subunit colored to emphasize secondary structure and domain organization. The N-terminal domain (bottom) is made up of the blue N-terminal loop and two long purple α helices (α1 and α2). The C-terminal α/β domain (top) is composed of five blue α helices (α3–α7) and three yellow β strands (β1–β3). The pink manganese lies between the two domains. MnSOD subunits have approximate dimensions 40 × 47 × 49 Å. (B) Active site geometry of MnSOD. The trigonal bipyramidal geometry of the five manganese ligands are drawn in a ball and stick representation. Amino acids from both domains contribute to the active site, His-26 and His-74 from the N-terminal domain and Asp-159 and His-163 from the C-terminal domain. The fifth coordination site is occupied by a water molecule (blue sphere).

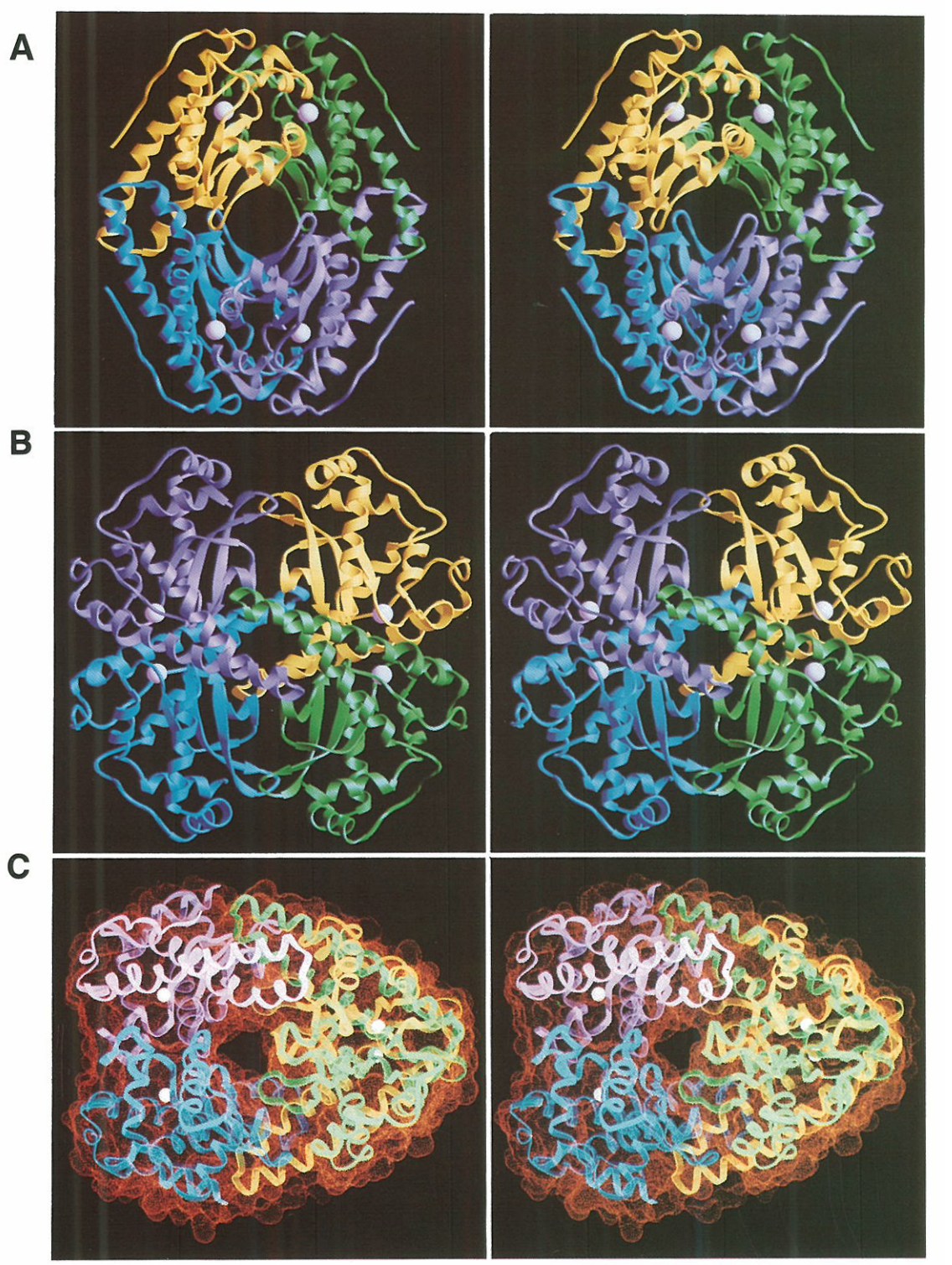

Figure 4. Assembly of the Human Mitochondrial MnSOD Tetramer

Stereo RIBBONS diagrams (Carson, 1991) of human MnSOD tetramer. Individual subunits are colored: A, yellow; B, green; C, blue; and D, purple. Manganese ions are shown as light pink spheres.

(A) The MnSOD tetramer viewed down the crystallographic **b** axis (with **a** vertical and **c** horizontal). The A/B (yellow/green) and C/D (blue/purple) dimers at the top and bottom of the figure each form a crystallographic asymmetric unit. The dimer interface (770 Å^2 buried) is arranged around a local molecular 2-fold symmetry axis, whereas the tetrameric assembly forms around the crystallographic 2-fold axis along the horizontal (**c** axis) and comprises the A/C (yellow/blue) and B/D (green/purple) 4-helix bundles (820 Å^2 buried) as well as the A/D (yellow/purple) and B/C (green/blue) cross-cavity interactions (190 Å^2 buried). The apparent central cavity is occluded (front and back) by the adjacent side chains of the cross-cavity interface. In this view the tetramer is rectangular with approximate dimensions of 60 Å wide, 79 Å high, and 79 Å deep.

(B) The MnSOD tetramer viewed down the crystallographic 2-fold axis along **c** (with **a** running diagonally from lower left to upper right and **b** from

structure critical for tetramer formation. Introns, taken from the rat gene (Ho et al., 1991), occur at Gly residues between α1 and α2 and also between α2 and α3 (Figure 1A), consistent with the separate domain structure for this region.

The C-terminal domain is a mixed α/β structure, with the central layer formed by a three-stranded antiparallel β sheet (residues 85–198). The first two helices of the C-terminal domain (α3 and α4) are separated by Gly-102 (ϕ = 80, ψ = −49; average values, see region C in Figure 1A), which causes an abrupt change in helical direction (~105°). Similarly, the C-terminal pair of helices, α6 and α7, are oriented approximately 100° to one another. Between them, in region J, Trp-181 has neither n + 3 or n + 4 helical hydrogen bonds; Asn-182 and Val-183 have 3_{10} hydrogen bonds; and Ile-184 adopts a β conformation. The central three-stranded antiparallel sheet has an "N-centered overhand" +1,−2x topology (Richardson and Richardson, 1990), with strands β2 and β3 separated by the short helical section α5. Helix α5 is separated from strand β3 only by Gly-151 (ϕ = 82, ψ = −9; average values). Strand β3 is followed by region H, a stretched helical structure with only two helical main-chain hydrogen bonds: an n + 3 hydrogen bond between 162O and 165N and an n + 4 hydrogen bond between 165O and 169N. Regions F and I are type II′ turns. A single intron occurs in the C-terminal domain at Gly-151 between α5 and β3 (Figure 1A).

The active site manganese joins the two domains and is positioned between the helical and β sheet structural elements (Figure 3B). Two amino acid residues from each domain, His-26 in α1 and His-74 in α2 from the N-terminal domain and Asp-159 in β3 and His-163 in region H from the C-terminal domain, plus a water molecule, ligate the Mn(II) with five-coordinate trigonal bipyramidal geometry. Manganese bond lengths are ~2.1 Å to each His $N^{\varepsilon 2}$, 1.94 Å to Asp-159 $O^{\delta 1}$, and 2.0 Å to the water. The four active sites of the MnSOD tetramer are grouped in pairs across the dimer interface (Figure 2,) with residues Glu-162 and Tyr-166 from one subunit contributing to the active site of the neighboring subunit.

Overall Quaternary Structure

The four identical subunits (A, yellow; B, green; C, blue; and D, purple) in the human MnSOD tetramer have 222 symmetry and assemble to form three unique pairs of interfaces (Figure 4): dimer interfaces (A/B and C/D), cross-cavity interfaces (A/D and B/C), and 4-helix bundle interfaces (A/C and B/D). Each asymmetric unit of the crystal contains one dimer (Figure 2), named for its similarity to the dimeric bacterial Fe and MnSODs. Two dimers, related by the crystallographic 2-fold axis of symmetry, form the homotetramer. The 4-helix bundle interfaces, together with the much smaller cross-cavity interfaces, join the dimers to form a tetramer. The solvent-filled tunnel through the center (Figure 4C) of the tetramer is encircled by the three-stranded antiparallel β sheets from the four subunits (Figure 5). The outside of the tetramer is encircled by the assembly of the four extended helical hairpins into two 4-helix bundles at opposite ends of the dimer. As a consequence of the central tunnel and subunit packing arrangement, the tetrameric mitochondrial MnSOD is held together almost entirely by two, rather than three, types of interfaces: the dimer contact and the 4-helix bundle contact.

In general, the participation of the dimer interface in the formation of the enzyme's active sites and of the tetrameric interface in stabilizing the helical hairpins (containing two of the manganese ligands) and in forming a larger active site channel suggests that only the tetrameric enzyme will be fully active and stable. The high thermostability of the wild-type tetrameric enzyme allows it to be purified by heat denaturation of contaminating proteins (see Experimental Procedures). The structural interactions responsible for the association of the four subunits into the active homotetrameric enzyme are described in more detail below.

Dimer Interface

The active site manganese atoms are located near the dimer interface (Figures 4A and 4B, subunits A/B [yellow and green] and C/D [blue and purple]), with residues from each subunit contributing to the metal-binding site. The dimer interactions (calculated using a 4.5 Å cutoff) involve residues from helices α1 (21, 25, 29–30), α2 (62–63, 65–66), and α6 (173), turns F (142) and I (170–171), and regions D (119–121) and H (161–163, 166–167). The surface buried to a 1.6 Å radius probe (Connolly, 1983) indicates that all 20 of these residues contribute more than 5 $Å^2$ of buried surface, for a total buried surface area of 770 $Å^2$ on each subunit. In the central region, the O^{γ} of Ser-121A is hydrogen bonded across the noncrystallographic 2-fold axis of symmetry to O^{γ} of Ser-121B. Slightly further from the axis, $O^{\varepsilon 1}$ of Glu-162A makes a hydrogen bond to the N of Glu-162B. Other salt bridges and hydrogen bonds that contribute to the dimer interface include $O^{\varepsilon 2}$ of Glu-162A to $N^{\delta 1}$ of His-163B (a manganese ligand), $O^{\varepsilon 1}$ of Glu-162A to N of His-163B, and $N^{\varepsilon 2}$ of His-30A to O^{γ} of Tyr-166B. Each of these interactions is duplicated by the noncrystallographic 2-fold symmetry axis.

Tetrameric Assembly

The human MnSOD dimer associates into a homotetramer with dimensions of about 60 × 79 × 79 Å. The central, solvent-filled tunnel, illustrated in Figure 4C, passes through the entire tetramer and has an average radius of

lower right to upper left). In this view the tetramer is square, with approximate dimensions of 71 Å by 71 Å and 58 Å deep. The 4-helix bundle interfaces form symmetrically from pairs of helical hairpins (B/D [green/purple] in front and A/C [yellow/blue] behind) across the 2-fold symmetry axis (center).

(C) The central cavity of human MnSOD tetramer is viewed 45° from the horizontal of (B). The red molecular surface was calculated using the MS program (Connolly, 1983) with a 1.4 Å probe radius.

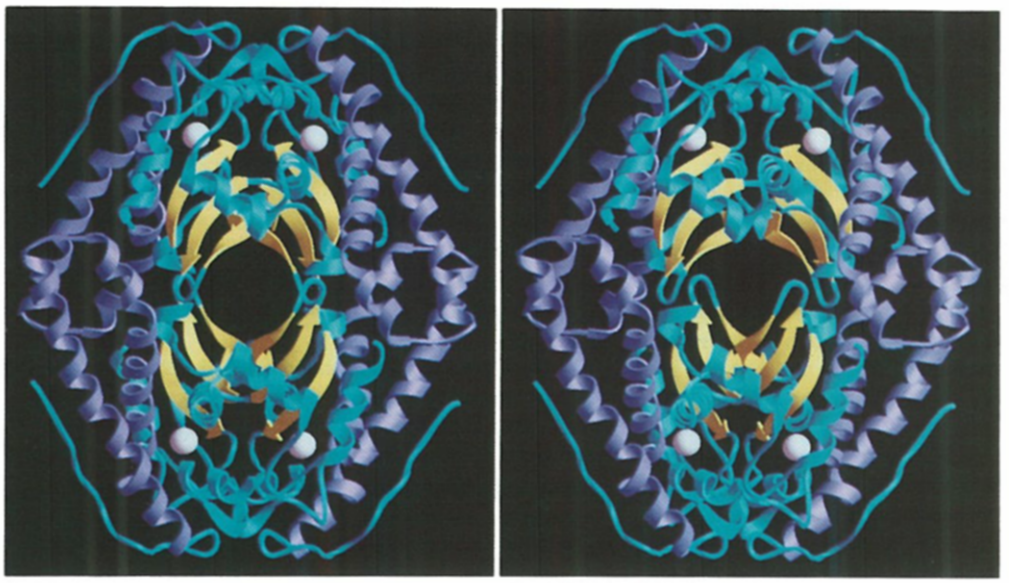

Figure 5. Arrangement of the Helical Hairpin and α/β Domains in the Assembled Tetramer

Stereo RIBBONS diagram viewed as in Figure 4A. Individual subunits are colored to highlight subunit domain positions in the assembled tetramer. The dominant tetrameric interaction comes from assembly of the N-terminal domains (purple helices and blue N-terminus) into two 4-helix bundles (left and right). The C-terminal domain (yellow β sheet and blue helices and loops) borders the central cavity. The dimer interfaces form across the top and bottom, and the cross-cavity interfaces form diagonally (at the front and back), in this view.

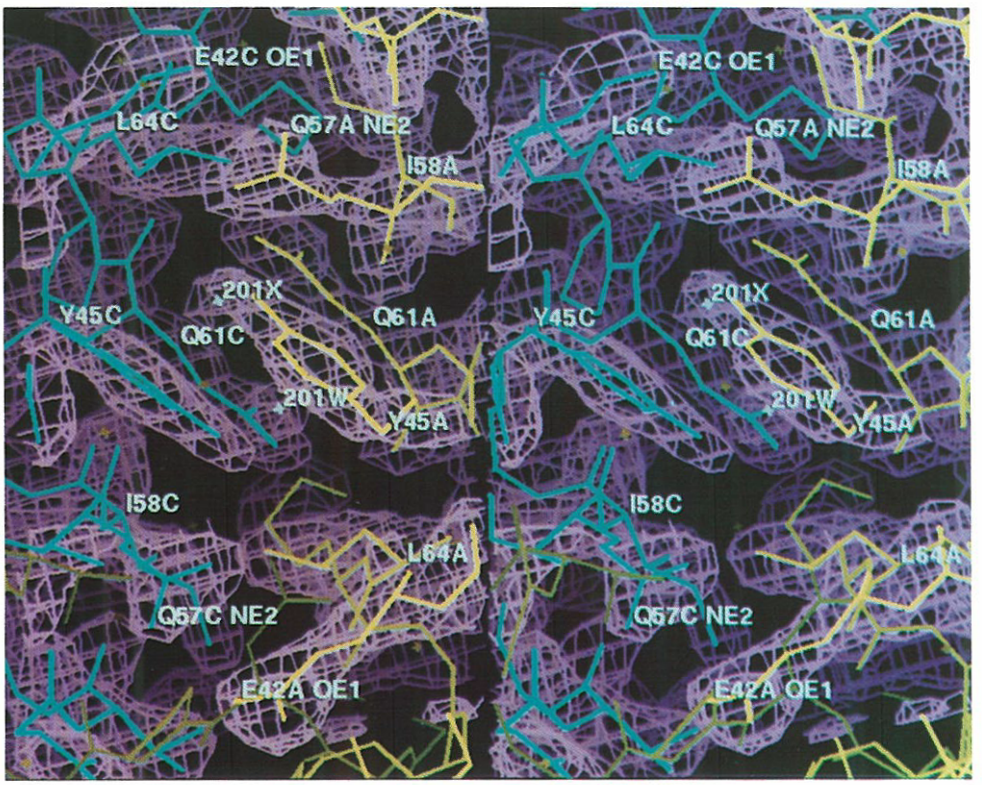

Figure 6. Electron Density and Model for the Central Residues within the 4-Helix Bundle Interface

A stereo diagram showing part of the central interactions of the 4-helix bundle placed in its $2F_o-F_c$ electron density (magenta contours). The model is colored as in Figure 4: A, yellow and C, blue. The view is close to the crystallographic 2-fold, which lies midway between the symmetry-related structural water molecules 201W and 201X. The α1A and α1C helices are in the foreground, and stacking interactions between these helices involve, in part, Y45A, Y45C, E42A, and E42C. Interactions between α2A and α2C are more extensive and involve, in part, residues Q57A, I58A, Q61A, L64A, Q57C, I58C, Q61C, and L64C. Two of the cross-helix interactions (between α1 and α2) involve hydrogen bonds from E42A to Q57C and E42C to Q57A. Image made using XtalView (McRee, 1992).

about three water molecules. The tetramer has an internal cavity (bordered by strand β2, as viewed in Figure 4A and Figure 5) with approximate dimensions of 15 × 25 Å at its widest point. When A/B and C/D dimers interact across the crystallographic 2-fold axis along **c** (Figure 4B), the cross-cavity and 4-helix bundle interfaces are formed. Therefore, each of the tetrameric interactions is duplicated by this 2-fold axis of symmetry.

In Figures 4A and 4B, residues from subunits A/D (yellow/purple) (and symmetry-related B/C [green/blue]) partially block the central cavity of the tetramer to form the small cross-cavity interface. Nine residues from secondary structural elements α3 (100–101), α4 (110), turn E (131–132), and β2 (134–137) interact with each other to bury about 190 Å^2 on each subunit. The N$^{\eta 2}$ of Arg-132A forms a hydrogen bond with the main-chain O of Leu-135D. The remaining interactions are van der Waals contacts.

In the principal tetrameric interface, the N-terminal α-helical hairpins of the A/C (yellow/blue) (and symmetry-related B/D [green and purple]; in Figures 4A and 4B) subunits assemble to form a 4-helix bundle with a left-handed twist. Twenty-four residues each contribute more than 5 Å^2 to this 820 Å^2 interface, which dominates the tetramer assembly (larger than each dimer interface that is 770 Å^2). Besides the 4-helix bundle interactions, some residues from the N-terminus and from helix α5 contribute interactions to this interface. In particular, the side chain of His-2A forms a hydrogen bond with the carbonyl oxygen of Gly-52C of turn A, and residues Pro-145A, Gln-147A, and Gly-148A of helix α5 interact with Thr-55C, Ile-58C, and Ala-59C of helix α2. The 4-helix bundle, however, forms the majority of this interface and is described in detail below.

The Intersubunit 4-Helix Bundle Interface

The 2-fold symmetric antiparallel interactions of the helical hairpins from two subunits form each of the two 4-helix bundle interfaces (see the purple helix bundles in Figure 5). This interface, which is unique to mitochondrial MnSOD, appears to be important not only for the enzyme's assembly but also for its stability and activity. In the subunit, if the helical hairpin is not tethered by formation of the 4-helix bundle, the two ligands contributed from helices α1 and α2 will be destabilized, adversely affecting the manganese active site geometry and the surrounding active site channel (which is formed between the helical hairpin and C-terminal domains). In addition, the tetrameric interaction forms the large solvent-filled tunnel open to the active site channels (Figure 4C). The tunnel is surrounded by positively charged side chains expected to aid in the recognition of superoxide, by analogy to the Cu,ZnSOD active site structure (Getzoff et al., 1992). For example, the tetrameric association positions a ring of 11 positively charged side chains around the subunit A active site: Lys-29A, Lys-44A, Lys-51A, Lys-130C, Lys-192C, Lys-106B, Lys-108B, Lys-110B, Lys-170B, Arg-173B, and Lys-178B. Thus, the 4-helix bundle strongly influences subunit structure, active site stability and conformation, tetrameric assembly, and substrate recognition.

The central residues of the 4-helix bundle are illustrated in Figure 6 along with their electron density. Eight residues from each subunit form the core of the interface (as indicated by their large average buried surface areas given in parentheses): Ile-58 (75 Å^2), Gln-61 (65 Å^2), Leu-49 (61 Å^2), Val-54 (57 Å^2), Thr-55 (52 Å^2), Tyr-45 (53 Å^2), Leu-64 (50 Å^2), and Ile-72 (45 Å^2). In the A/C interface (yellow/blue in Figures 4A and 4B), for example, the side chains of the α1 helices of subunit A and subunit C interact in an antiparallel fashion with the crystallographic 2-fold axis of symmetry between Tyr-45A and Tyr-45C (see Figure 6). The side chains of residues Glu-42, Tyr-45, Gln-46, and Leu-49 stack across the subunit–subunit interface in an antiparallel manner (data not shown). The subunit–subunit interactions involving antiparallel contacts between helix α2A and helix α2C are more extensive. Residues Gly-52, Val-54, Thr-55, Gln-57, Ile-58, Gln-61, Leu-64, Lys-65, Gly-68, Gly-69, and Ile-72 of helix α2 stack across the interface with the crystallographic 2-fold axis of symmetry between Gln-61A and Gln-61C. The side chain of Gln-61A forms a hydrogen bond with the carbonyl oxygen of Gln-61C across the interface (Figure 6). Cross-helix interactions are formed by residues Leu-38A and Glu-42A of helix α1 interacting with residues Gly-52C, Val-54C, and Gln-57C of helix α2 and vice versa. The O$^{\varepsilon 1}$ of Glu-42A and N$^{\varepsilon 2}$ of Gln-57C form a hydrogen bond. Two water molecules (about 3 Å apart), related to each other by the 2-fold axis of symmetry, are buried in the 4-helix bundle. These structural water molecules (temperature factor of 17.5 Å^2) form hydrogen bonds with the O$^{\eta}$ of Tyr-45 and the N$^{\varepsilon 2}$ of Gln-61 (Figure 6).

To test the apparent similarity of the two equivalent MnSOD intersubunit 4-helix bundles to 4-helix bundles found within protein subunits, one MnSOD 4-helix bundle was superimposed onto that of tobacco mosaic virus coat protein (TMVcp) (Figure 7). Unlike the helices of TMVcp, which are fairly straight, two helices of the MnSOD bundle are bent at Pro-62, limiting the optimum superposition of all four helices. When the main-chain atoms of the two straight α1 helices are superimposed (labeled A and D in Figure 7), the root mean square deviation is only 1.59 Å as compared with 2.25 Å when all four helices are superimposed. Nevertheless, the overall dimensions and geometry of MnSOD intersubunit 4-helix bundles are remarkably similar to that of the TMVcp 4-helix bundle subunit folding domain.

An intersubunit 4-helix bundle assembly with symmetrical helical hairpins has been seen before in the structure of the E. coli Rop protein (Banner et al., 1987). However, the Rop protein is only 63 aa long, and the dimeric interface formed by its association into a 4-helix bundle involves the entire protein. In the MnSOD tetramer assembly, the extension of the N-terminal helical hairpins allows the formation of a stable tetrameric enzyme by using a portion of the subunit sequence.

Comparison with the Bacterial Enzyme Structures

There are four structures published for the bacterial Fe and MnSODs: T. thermophilus tetrameric MnSOD at 1.8 Å resolution (Ludwig et al., 1991), B. stearothermophilus dimeric MnSOD at 2.4 Å resolution (Parker and Blake, 1988), E. coli dimeric FeSOD at 3.1 Å resolution (Carlioz et

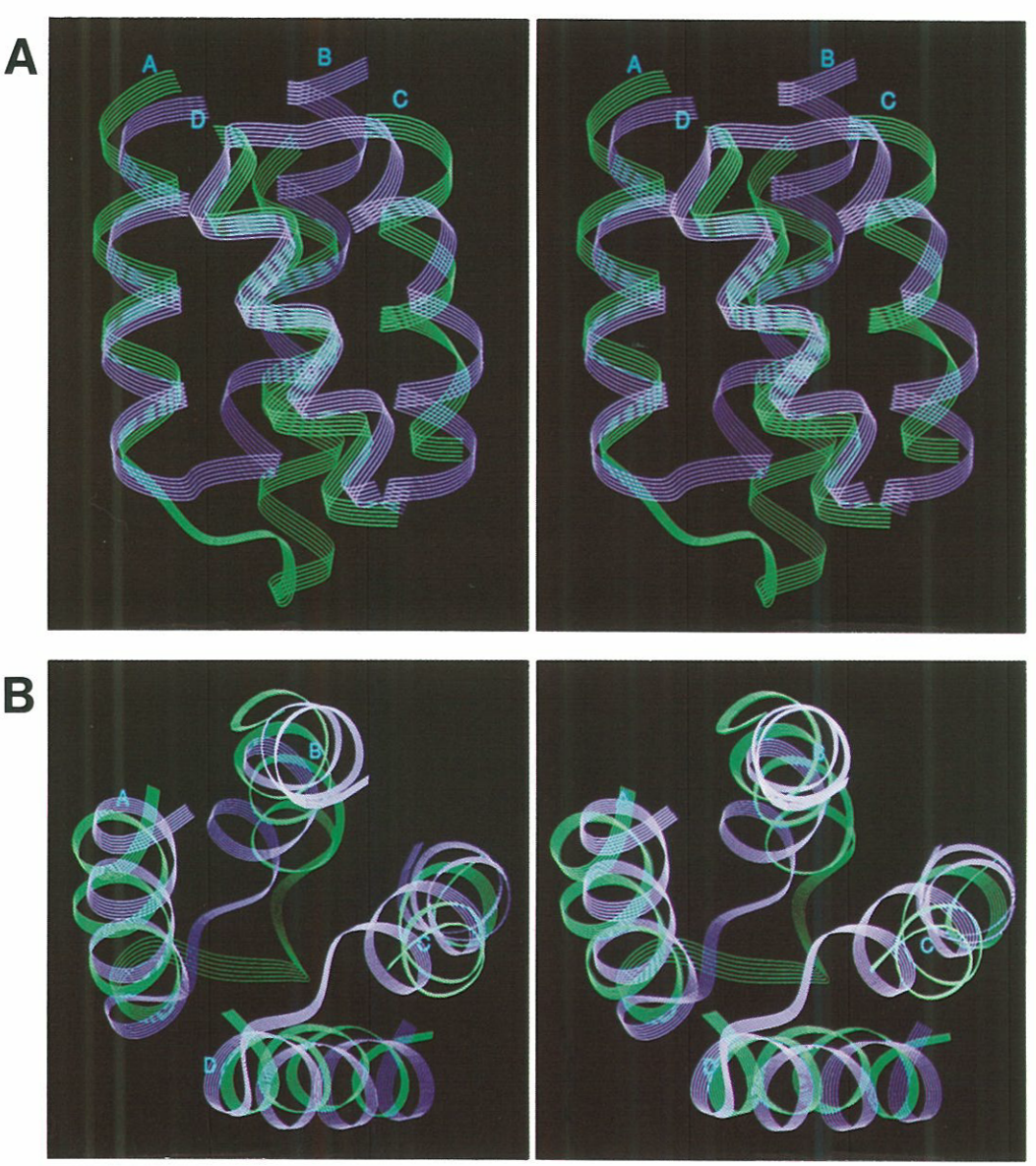

Figure 7. Comparison of the Intersubunit 4-Helix Bundle Interface with the 4-Helix Bundle of TMVcp

MnSOD 4-helix bundle (purple) superimposed onto the 4-helix bundle of tobacco mosaic virus coat protein (green, TMVcp) (Protein Data Bank entry, 2tmv; Namba et al., 1989; Bernstein et al., 1977). Stereo diagrams of (A) side view and (B) top view. Main-chain atoms of the following residues were superimposed (root mean square deviation, 2.25 Å) in the displayed helix pairs: A, MnSOD 39–49 onto TMVcp 21–31; B, MnSOD 54–64 onto TMVcp 41–51; C, MnSOD 54–64 onto TMVcp 76–86; and D, MnSOD 39–49 onto TMVcp 119–129. The overall similarity of bundle dimensions and helix packing is apparent.

al., 1988), and P. ovalis dimeric FeSOD at 2.1 Å resolution (Stoddard et al., 1990a). Each subunit of these bacterial SODs, like those of human MnSOD, is structurally divided into N- and C-terminal domains, although the domain description for P. ovalis places the helix that is equivalent to human MnSOD helix α2 in the C-terminal domain. Otherwise, all five C-terminal domains are structurally similar. In the bacterial SOD structures, the N-terminal helices are much shorter than those in the human helical hairpin, and the longer, sequence-variable (Beyer et al., 1991), intervening region includes a short helix.

The active site region (Figure 3B) and the dimer interface (Figure 2) are structurally conserved with small variations between human MnSOD and the bacterial Mn and FeSODs. One interesting dimer interface variation involves the human MnSOD packing interactions of Phe-66A with Gln-119B compared with the similar but inverted interactions of Asn-75A with Phe-128B in the bacterial enzyme structures. The active site metals in the Mn and FeSOD structures all have four protein ligands (3 His and 1 Asp) in distorted tetrahedral geometry, which can also be described as trigonal bipyramidal when the open coor-

dination site is included. The fifth ligand water molecule (2 Å from the manganese) in human MnSOD was also observed in T. thermophilus MnSOD. In human and T. thermophilus MnSOD, the dimer interface places the two metal ions about 18.4 Å apart, and in P. ovalis FeSOD they are 17.9 Å apart. In all the structures, the ligand hydrogen bonding network includes hydrogen bonds spanning the dimer interface, from a His ligand in one subunit to a Glu carboxylate in the other, such that both subunits contribute to the metal-binding site.

Tetramer formation is a characteristic of both human and thermostable bacterial MnSODs (Beyer et al., 1991), but the nature of their tetrameric assemblies is very different. The human MnSOD tetramer is more compact than that determined for T. thermophilus MnSOD, as exemplified by intermanganese distances. Manganese distances between the A/C and A/D subunits in human MnSOD are 40.7 Å and 42.0 Å, respectively, whereas T. thermophilus MnSOD has significantly longer intermanganese distances of 45.4 Å and 48.9 Å. This difference in overall tetramer size is derived from the most dramatic difference between human and T. thermophilus MnSOD subunit structure: the human MnSOD N-terminal helical hairpins. The human MnSOD tetramer interface is formed by the association of the helical hairpin N-terminal domains into closely packed, intersubunit 4-helix bundles, whereas the T. thermophilus interface involves loop regions with typical protein subunit packing interactions. Thus, the cross-cavity packing interactions that occur between nonadjacent subunits in the more compact human MnSOD tetramer do not occur in the T. thermophilus MnSOD structure.

Significance and Implications

In contrast to bacterial Fe and MnSODs, human mitochondrial MnSOD forms two interchain, 4-helix bundle, tetrameric interfaces (Figure 7), symmetrically assembled from pairs of N-terminal helical hairpins (Figure 4). Each of these helices is encoded by a separate exon, with adjacent intron–exon junctions mapping to surface loops (Figure 1A). Thus, the gene encoding the mitochondrial tetrameric enzyme may have evolved by addition of these exons to the gene for the postulated ancestral dimer. The self-assembly of helical hairpin domains into interchain 4-helix bundles could be generally applicable to the design of new, multimeric, recombinant proteins.

Structurally, the helical hairpin of human MnSOD contributes not only to the tetramer assembly (Figure 4) but also to the conformation of the active site, located between the helical hairpin and α/β domains (Figure 3). The sequence of the helical hairpin is highly conserved in mitochondrial MnSODs (Smith and Doolittle, 1992), supporting its functional importance. Yet, human MnSOD is polymorphic (Figure 1A), and one naturally occurring variant in the helical hairpin (Ile-58 to Thr) has been found in two of six cDNA libraries (Wispe et al., 1989; Ho and Crapo, 1988). Within the 4-helix bundle interface (Figure 6), hydrophobic residue Ile-58 is the largest contributor of buried surface area, contacting 6 other residues. Replacement with hydrophilic Thr-58 should destabilize the 4-helix bundle, leading to decreased enzyme activity and reduced tetramer stability. Furthermore, the detrimental effect of each single-site Thr-58 mutation within the 4-helix bundle should be quadrupled in the tetrameric enzyme due to the duplication and 2-fold internal symmetry of the 4-helix bundle. Preliminary biochemical experiments support this structure-based prediction: the Thr-58 MnSOD variant is significantly less active and less thermostable (M. Boissinot, M. J. Johnson, J. A. Tainer, and R. A. Hallewell, unpublished data). Moreover, significant variation in specific enzyme activity and overall activity is found in human liver samples (Deutsch et al., 1991), demonstrating biologically relevant MnSOD variability.

MnSOD variants may exhibit balanced polymorphism like that of human hemoglobin, in which a structurally and functionally defective single-site mutant (sickle cell hemoglobin) (Ingram, 1957) is maintained in the population due to a compensatory advantage (malarial resistance) (Allison, 1956; Stine et al., 1992). Two-fold reduced MnSOD activity significantly increases the cytotoxic action of tumor necrosis factor by increasing mitochondrial superoxide levels (Wong et al., 1989), and tumor necrosis factor kills virus-infected cells (Nain et al., 1990). An unfortunate side effect of an initial selection for MnSOD variants with reduced activity and increased protection against acute viral infections might be a predisposition for diseases, such as diabetes (Malaisse et al., 1982; Crouch et al., 1981), that are associated with oxidative damage. Mitochondria are especially sensitive to oxidative damage, and mitochondrial DNA damage is implicated in aging and degenerative conditions, including Alzheimer's and Parkinson's diseases (Taylor, 1992; Wallace, 1992), as well as in diabetes (Ballinger et al., 1992). MnSOD with decreased activity is found in leukocytes of diabetics (Nath et al., 1984), and SOD is protective of healthy pancreatic islet tissue transplanted into diabetic animals (Nomikos et al., 1989). In addition, juvenile onset diabetes may be triggered by viral infection in genetically susceptible individuals (Yoon, 1990), and tumor necrosis factor (generated in response to infections) is cytotoxic to islet cells (Campbell et al., 1988). Thus, reduced MnSOD activity may confer an early selective advantage by enhancing cellular defenses against viral diseases and cancers at the cost of reduced protection against long-term oxidative damage. This new three-dimensional structure of human MnSOD should provide improved understanding of the structural basis for SOD activity and for the effect of polymorphic sequence variation on mitochondrial SOD structure and function.

Experimental Procedures

Expression and Purification

The full-length MnSOD cDNA was isolated from a library of human kidney cDNAs cloned into bacteriophage lambda (Bell et al., 1986), using the mouse MnSOD cDNA (Hallewell et al., 1986) as a hybridization probe. The sodAsodB strain of E. coli (Natvig et al., 1987), which lacks the endogenous Mn and FeSODs, was used to avoid the possibility of heterotetramer formation between the human enzyme and the endogenous E. coli enzymes. Cells transformed with an E. coli expression vector containing the cDNA (pcHMnSOD1laclq) produced up to 25% of total soluble cell protein as human MnSOD, yielding approximately 40 mg of purified enzyme per liter of culture. Culture conditions and the procedure for inducing the tacI promoter of pcHMnSOD1laclq

in the E. coli sodAsodB strain were as previously described (Hallewell et al., 1985). This was followed by a rapid protein purification procedure (Beck et al., 1988) as follows: after cell lysis, soluble cell proteins were heated at 60°C for 60 min; precipitated proteins were removed by centrifugation; and the supernatant was purified on DE52 and CM52 columns, consecutively. We have purified to homogeneity large amounts of wild-type recombinant human MnSOD that has normal specific activity and appears indistinguishable from the native enzyme purified from human tissue (W. F. Beyer, G. I. Bell, R. A. Hallewell, and I. Fridovich, unpublished data).

Crystallization

Several crystal forms of recombinant human MnSOD crystals were grown using polyethylene glycol (PEG) 400, 600, 4000, and 10000, ammonium sulfate, potassium phosphate, and citrate as precipitating agents. The protein concentration for these experiments was 10 mg/ml buffered in 50 mM phosphate (pH 7.8). Crystals obtained with 2.1–2.3 M potassium phosphate at pH 7.0 grew within 7 days as long, hexagonal rhombs (0.3 × 0.3 × 1.0 mm^3). These crystals belong to space group $P6_122$ (or $P6_522$) with cell dimensions of a = b = 80.9 Å, c = 240.3 Å. On the basis of crystal symmetry, cell dimensions, and a molecular weight of 22,000, a V_m of 2.58 $Å^3$ per dalton was obtained for one dimer in the asymmetric unit, corresponding to a solvent content of 52% (Matthews, 1968). Crystals grown from 1.5 M citrate at pH 8.5 (0.1 × 0.05 × 0.2 mm^3) appeared within 7 days and were morphologically similar to the phosphate-grown crystals. Crystals grown from 15% PEG 600 required 30 days and grew as long thin needles (0.1 × 0.1 × 1.0 mm^3), while those from 20% PEG 4000, 10% 2-propanol at pH 7.5, or from 21.5% PEG 10000 at pH 7.5 appeared within 7 days as rosettes of thin needles. Crystals obtained with ammonium sulfate as precipitant grew as thin plates (0.05 × 0.1 × 0.1 mm^3), and precession photography shows diffuse Bragg reflections at low resolution, indicating disorder in these crystals. Crystals grown from 24%–30% PEG 400 grew within 3–5 days as long needles (0.2 × 0.1 × 1.0 mm^3) or as short rhombs (0.2 × 0.2 × 0.4 mm^3) and belong to the space group $P2_12_12$ with cell dimensions a = 76.13 Å, b = 79.90 Å, c = 68.05 Å (V_m = 2.34 $Å^3$ per dalton for one dimer in the asymmetric unit and solvent content of 47%). Crystals grown from PEG 4000 in the absence of 10% propanol were larger than and isomorphous with the PEG 400 crystals. Optimization of several of the crystal forms described above provided crystals suitable for high resolution data collection. These comprehensive screens reproduced crystal forms independently identified by others (Deutsch et al., 1991; Matsuda et al., 1990; Wagner et al., 1989; Beem et al., 1976). We report here the atomic structure determined for the human MnSOD enzyme in the $P2_12_12$ crystal form grown from PEG 400.

Data Collection

Data were collected at room temperature from one crystal (0.25 × 0.2 × 0.5 mm^3) on a Siemens area detector. The program package XENGEN (Howard et al., 1987) was used for data reduction. A total of 19,738 unique reflections (117,362 total measurements) were collected, representing 92% of the possible data out to a resolution of 2.2 Å. The data are 99% complete to 2.3 Å resolution and 52% complete in the 2.2–2.3 Å shell. The R_{symm} on intensities was 9%.

Structure Solution and Refinement

Initial phases were solved by molecular replacement with the MERLOT (Fitzgerald, 1988) and XPLOR (Brünger et al., 1987) program packages using a dimer of bacterial superoxide dismutase as the probe. Probes derived from Thermus thermophilus MnSOD (Ludwig et al., 1991) and Pseudomonas ovalis FeSOD (Stoddard et al., 1990b) gave similar solutions (R factors of 47% and 50%, respectively). Metal ions were not included in the search probes to provide a check for the molecular replacement phases. Further refinement was performed using the higher resolution coordinates of Thermus thermophilus MnSOD. Rigid body refinement, carried out with the MnSOD probe using XPLOR, reduced the R factor to 44.4%. The sequence was humanized, substituting Ala where there were steric conflicts, and subjected to one round of simulated annealing refinement using the "slow cooling protocol" (Brünger et al., 1990), followed by one round of conventional refinement. This reduced the R factor to 25.5% for 3σ data between 10 Å and 2.5 Å resolution. Noncrystallographic symmetry was not restrained. Most of the atomic model was fit to "simulated annealing omit" Fourier maps, and the manganese atoms were placed in the active sites. The electron density for residues 45–60 was uninterpretable, so this segment was not included in the atomic model. The subsequent round of refinement reduced the R factor to 22.9%. After three cycles of fitting and refinement, the entire protein fold was interpreted, and the R factor was 19.3%. The electron density of the C-terminal dipeptide was partially disordered. Water molecules were automatically added to the atomic model by searching an F_o–F_c map and identifying peaks that were potential water molecules. After refinement, each water was visually reviewed, and those that refined with high temperature factors or occupied the electron density of a disordered amino acid side chain were deleted. In the last stage of refinement, the resolution was extended to 2.2 Å, and another round of water addition resulted in an R factor of 17.1%. The final atomic model consists of 3146 nonhydrogen protein atoms, 2 manganese atoms, and 169 water molecules. The overall deviations from ideal geometry were 0.018 Å for bond distances and 3.3° for bond angles. The protein atomic model had an average temperature factor of 25.2 $Å^2$. The average temperature factor of water molecules was 38.8 $Å^2$ (standard deviation, 13.2) with a minimum of 8.0 $Å^2$ and a maximum of 59.7 $Å^2$. Coordinates were submitted to the Protein Data Bank (code 1ABM).

Acknowledgments

This work was supported by National Institutes of Health grant GM39345. We thank Elizabeth Getzoff, Duncan McRee, Irwin Fridovich, Maurice Boissinot, Michael Pique, and Brian Crane for their intellectual contributions. We thank Dagmar Ringe and Barry Stoddard for the P. ovalis FeSOD coordinates and Martha Ludwig and William Stallings for the T. thermophilus MnSOD coordinates.

The costs of publication of this article were defrayed in part by the payment of page charges. This article must therefore be hereby marked *"advertisement"* in accordance with 18 USC Section 1734 solely to indicate this fact.

Received June 30, 1992; revised August 12, 1992.

References

Adelman, R., Saul, R. L., and Ames, B. N. (1988). Oxidative damage to DNA: relation to species metabolic rate and life span. Proc. Natl. Acad. Sci. USA *85*, 2706–2708.

Allison, A. C. (1956). Sickle cells and evolution. Sci. Am. *195*, 87–94.

Ames, B. N. (1983). Dietary carcinogens and anticarcinogens. Oxygen radicals and degenerative diseases. Science *221*, 1256–1264.

Ballinger, S. W., Shoffner, J. M., Hedaya, E. V., Trounce, I., Polak, M. A., Koontz, D. A., and Wallace, D. C. (1992). Maternally transmitted diabetes and deafness associated with a 10.4 kb mitochondrial DNA deletion. Nature Genet. *1*, 11–17.

Banner, D. W., Kokkinidis, M., and Tsernoglou, D. (1987). Structure of the ColE1 rop protein at 1.7 Å resolution. J. Mol. Biol. *196*, 657–675.

Beck, Y., Oren, R., Amit, B., Levanon, A., Gorecki, M., and Hartman, J. R. (1987). Human Mn superoxide dismutase cDNA sequence. Nucl. Acids Res. *15*, 9076.

Beck, Y., Bartfeld, D., Yavin, Z., Levanon, A., Gorecki, M., and Hartman, J. R. (1988). Efficient production of active human manganese superoxide dismutase in *Escherichia coli*. Biotechnology *6*, 930–935.

Beem, K. M., Richardson, J. S., and Richardson, D. C. (1976). Manganese superoxide dismutases from *Escherichia coli* and from yeast mitochondria: preliminary X-ray crystallographic studies. J. Mol. Biol. *105*, 327–332.

Bell, G. I., Najarian, R. C., Mullenbach, G. T., and Hallewell, R. A. (1986). cDNA sequence coding for human kidney catalase. Nucl. Acids Res. *14*, 5561–5562.

Bernstein, F. C., Koetzle, T. F., Williams, G. J. B., Meyer, E. F., Jr., Brice, M. D., Rodgers, J. R., Kennard, O., Shimanouchi, T., and Tasumi, M. (1977). The Protein Data Bank: a computer-based archival file for macromolecular structures. J. Mol. Biol. *112*, 535–542.

Beyer, W. F., Jr., and Fridovich, I. (1987). Effect of hydrogen peroxide

on the iron-containing superoxide dismutase of *Escherichia coli*. Biochemistry *26*, 1251–1257.

Beyer, W., Imlay, J., and Fridovich, I. (1991). Superoxide dismutases. Prog. Nucleic Acid Res. Mol. Biol. *40*, 221–253.

Brünger, A. T., Kuriyan, J., and Karplus, M. (1987). Crystallographic R-factor refinement by molecular dynamics. Science *235*, 458–460.

Brünger, A. T., Krukowski, A., and Erickson, J. W. (1990). Slow-cooling protocols for crystallographic refinement by simulated annealing. Acta Crystallogr. A *46*, 585–593.

Campbell, I. L., Iscaro, A., and Harrison, L. C. (1988). IFN-γ and tumor necrosis factor-α cytotoxicity to murine islets of langerhans. J. Immunol. *141*, 2325–2329.

Carlioz, A., Ludwig, M. L., Stallings, W. C., Fee, J. A., Steinman, H. M., and Touati, D. (1988). Iron superoxide dismutase nucleotide sequence of the gene from *Escherichia coli K12* and correlations with crystal structures. J. Biol. Chem. *263*, 1555–1562.

Carson, M. (1991). RIBBONS 2.0. J. Appl. Crystallogr. *24*, 958–961.

Cerutti, P. A. (1985). Prooxidant states and tumor production. Science *227*, 375–381.

Chance, B., Sies, H., and Boveris, A. (1979). Hydroperoxide metabolism in mammalian organs. Physiol. Rev. *59*, 527–605.

Church, S. L. (1990). Manganese superoxide dismutase: nucleotide and deduced amino acid sequence of a cDNA encoding a new human transcript. Biochem. Biophys. Acta *1087*, 250–252.

Connolly, M. L. (1983). Analytical molecular surface calculation. J. Appl. Crystallogr. *16*, 548–558.

Crouch, R. K., Gandy, S. E., Kimsey, G., Galbraith, R. A., Galbraith, G. M. P., and Buse, M. G. (1981). The inhibition of islet superoxide dismutase by diabetogenic drugs. Diabetes *30*, 235–241.

Deutsch, H. F., Hoshi, S., Matsuda, Y., Suzuki, K., Kawano, K., Kitagawa, Y., Katsube, Y., and Taniguchi, N. (1991). Preparation of human manganese superoxide dismutase by tri-phase partitioning and preliminary crystallographic data. J. Mol. Biol. *219*, 103–108.

Fitzgerald, P. M. D. (1988). MERLOT, an integrated package of computer programs for the determination of crystal structures by molecular replacement. J. Appl. Crystallogr. *21*, 273–278.

Floyd, R. A. (1991). Oxidative damage to behavior during aging. Science *234*, 1597.

Fraga, C. G., Shigenaga, M. K., Park, J.-W., Degan, P., and Ames, B. N. (1990). Oxidative damage to DNA during aging: 8-hydroxy-2′-deoxyguanosine in rat organ DNA and urine. Proc. Natl. Acad. Sci. USA *87*, 4533–4537.

Fridovich, I. (1986). Superoxide dismutases. Adv. Enzymol. *58*, 61–97.

Getzoff, E. D., Cabelli, D. E., Fisher, C. L., Parge, H. E., Viezzoli, M. S., Banci, L., and Hallewell, R. A. (1992). Faster superoxide dismutase mutants designed by enhancing electrostatic guidance. Nature *358*, 347–351.

Gorecki, M., Beck, Y., Hartman, J. R., Fischer, M., Weiss, L., Tochner, Z., Slavin, S., and Nimrod, A. (1991). Recombinant human superoxide dismutases: production and potential therapeutical uses. Free Radic. Res. Commun. *1*, 401–410.

Hallewell, R. A., Masiarz, F. R., Najarian, R. C., Puma, J. P., Quiroga, M. R., Randolph, A., Sanchez-Pescador, R., Scandella, C. J., Smith, B., Steimer, K. S., and Mullenbach, G. T. (1985). Human Cu/Zn superoxide dismutase cDNA: isolation of clones synthesizing high levels of active or inactive enzyme from an expression library. Nucl. Acids Res. *13*, 2017–2034.

Hallewell, R. A., Mullenbach, G., Stempien, M., and Bell, G. (1986). Sequence of a cDNA coding for mouse manganese superoxide dismutase. Nucl. Acids Res. *14*, 9539.

Hallewell, R. A., Laria, I., Tabrizi, A., Carlin, G., Getzoff, E. D., Tainer, J. A., Cousens, L. S., and Mullenbach, G. T. (1989). Genetically engineered polymers of human CuZn superoxide dismutase. J. Biol. Chem. *264*, 5260–5268.

Halliwell, B., and Gutteridge, J. M. C. (1989). Free Radicals in Biology and Medicine (Oxford: Clarendon Press), pp. 22–408.

Halliwell, B., Gutteridge, J. M. C., and Blake, D. (1985). Metal ions and oxygen radical reactions in human inflammatory joint disease. Phil. Trans. Roy. Soc. (Lond.) B *311*, 659–671.

Harman, D. (1981). The aging process. Proc. Natl. Acad. Sci. USA *78*, 7124–7128.

Hassan, H. M. (1988). Biosynthesis and regulation of superoxide dismutases. Free Radic. Biol. Med. *5*, 377–385.

Heckl, K. (1988). Isolation of cDNAs encoding human manganese superoxide dismutase. Nucl. Acids Res. *16*, 6224.

Ho, Y. S., and Crapo, J. D. (1988). Isolation and characterization of complementary DNAs encoding human manganese-containing superoxide dismutase. FEBS Lett. *229*, 256–260.

Ho, Y. S., Howard, A. J., and Crapo, J. D. (1991). Molecular structure of a functional rat gene for manganese-containing superoxide dismutase. Am. J. Respir. Cell Mol. Biol. *4*, 278–286.

Housset, B., and Junod, A. P. (1981). Enzyme response of cultured endothelial cells to hyperoxia. Bull. Eur. Physiopathol. Respir. *17*, 107–110.

Howard, A. J., Gilliland, G. L., Finzel, B. C., Poulos, T. L., Ohlendorf, D. H., and Salemme, F. R. (1987). The use of an imaging proportional counter in macromolecular crystallography. J. Appl. Crystallogr. *20*, 383–387.

Ingram, V. M. (1957). Gene mutations in human hemoglobin: the chemical difference between normal and sickle cell hemoglobin. Nature *180*, 326–328.

Kirby, T. W., Lancaster, J., Jr., and Fridovich, I. (1981). Isolation and characterization of the iron-containing superoxide dismutase of *Methanobacterium bryantii*. Arch. Biochem. Biophys. *210*, 140–148.

Krall, J., Bagley, A. C., Mullenbach, G. T., Hallewell, R. A., and Lynch, R. E. (1988). Superoxide mediates the toxicity of paraquat for cultured mammalian cells. J. Biol. Chem. 263, 1910–1914.

Ludwig, M. L., Metzger, A. L., Pattridge, K. A., and Stallings, W. C. (1991). Manganese superoxide dismutase from *Thermus thermophilus*: a structural model refined at 1.8 Å resolution. J. Mol. Biol. *219*, 335–358.

Malaisse, W. J., Malaisse-Lagae, F., Sener, A., and Pipeleers, D. G. (1982). Determinants of the selective toxicity of alloxan to the pancreatic B cell. Proc. Natl. Acad. Sci. USA *79*, 927–930.

Masuda, A., Longo, D. L., Kobayashi, Y., Appella, E., Oppenheim, J. J., and Matsusima, K. (1988). Induction of mitochondrial manganese superoxide dismutase by interleukin 1. FASEB J. *2*, 3087–3091.

Matsuda, Y., Higashiyama, S., Kijima, Y., Suzuki, K., Kawano, K., Akiyama, M., Kawata, S., Tarui, S., Deutsch, H. F., and Taniguchi, N. (1990). Human liver manganese superoxide dismutase. Purification and crystallization, subunit association and sulfhydryl reactivity. Eur. J. Biochem. *194*, 713–720.

Matthews, B. W. (1968). Solvent content in protein crystals. J. Mol. Biol. *33*, 491–497.

McRee, D. E. (1992). A visual protein crystallographic software system for X11/Xview. J. Graphics Mol. *10*, 44–46.

McRee, D. E., Redford, S. M., Getzoff, E. D., Lepock, J. R., Hallewell, R. A., and Tainer, J. A. (1990). Changes in crystallographic structure and thermostability of a Cu,Zn superoxide dismutase mutant resulting from removal of a buried cysteine. J. Biol. Chem. *265*, 14234–14241.

Murohara, Y., Yui, Y., Hattori, R., and Kawai, C. (1991). Effects of superoxide dismutase on reperfusion arrhythmias and left ventricular function in patients undergoing thrombolysis for anterior wall acute myocardial infarction. Am. J. Cardiol. *67*, 765–767.

Nain, M., Hinder, F., Gong, J. H., Schmidt, A., Bender, A., Sprenger, H., and Gemsa, D. (1990). Tumor necrosis factor-alpha production of influenza a virus-infected macrophages and potentiating effect of lipopolysaccharides. J. Immunol. *145*, 1921–1928.

Nakazono, K., Watanabe, N., Matsuno, K., Sasaki, J., Sato, T., and Inoue, M. (1991). Does superoxide underlie the pathogenesis of hypertension? Proc. Natl. Acad. Sci. USA *88*, 10045–10048.

Namba, K., Pattanayek, R., and Stubbs, G. (1989). Visualization of protein-nucleic acid interactions in a virus: refined structure of intact tobacco mosaic virus at 2.9 Å resolution by X-ray fiber diffraction. J. Mol. Biol. *208*, 307–325.

Nath, N., Chari, S. N., and Rathi, A. B. (1984). Superoxide dismutase in diabetic polymorphonuclear leukocytes. Diabetes *33*, 586–589.

Natvig, D., Imlay, K., Touati, D., and Hallewell, R. A. (1987). Human copper-zinc superoxide dismutase complements superoxide dismutase deficient *E. coli* mutants. J. Biol. Chem. *262*, 14697–14701.

Niwa, Y., Ishimoto, K., and Kanoh, T. (1990). Induction of superoxide dismutase in leukocytes by paraquat: correlation with age and possible predictor of longevity. Blood *76*, 835–841.

Nomikos, I. N., Wang, Y., and Lafferty, K. J. (1989). Involvement of O_2 radicals in 'autoimmune' diabetes. Immunol. Cell Biol. *67*, 85–87.

Oberley, L. W., Clair, D. K. S., Autor, A. P., and Oberley, T. D. (1987). Increase in manganese superoxide dismutase activity in the mouse heart after X-irradiation. Arch. Biochem. Biophys. *254*, 69–80.

Oda, T., Akaike, T., Hamamoto, T., Suzuki, F., Hirano, T., and Maeda, H. (1989). Oxygen radicals in influenza-induced pathogenesis and treatment with pyran polymer-conjugated SOD. Science *244*, 974–976.

Parge, H. E., Hallewell, R. A., and Tainer, J. A. (1992). Atomic structures of wild-type and thermostable mutant recombinant human Cu,Zn superoxide dismutase. Proc. Natl. Acad. Sci. USA *89*, 6109–6113.

Parker, M. W., and Blake, C. C. F. (1988). Crystal structure of manganese superoxide dismutase from *Bacillus stearothermophilus* at 2.4 Å resolution. J. Mol. Biol. *199*, 649–661.

Ramachandran, G. N., and Sasisekharan, V. (1968). Conformation of polypeptides and proteins. Adv. Protein Chem. *23*, 283–437.

Reveillaud, I., Niedzwiecki, A., Bensch, K. G., and Fleming, J. E. (1991). Expression of bovine superoxide dismutase in *Drosophila melanogaster* augments resistance to oxidative stress. Mol. Cell. Biol. *11*, 632–640.

Richardson, J. S., and Richardson, D. C. (1990). Principles and patterns of protein conformation. In Prediction of Protein Structure and the Principles of Protein Conformation, G. D. Fasman, ed. (New York: Plenum Publishing Corp.), pp. 1–98.

Richter, C., Park, J., and Ames, B. N. (1988). Normal oxidative damage to mitochondrial and nuclear DNA is extensive. Proc. Natl. Acad. Sci. USA *85*, 6465–6467.

St. Clair, D. K., and Holland, J. C. (1991). Complementary DNA encoding human colon cancer manganese superoxide dismutase and the expression of its gene in human cells. Cancer Res. *51*, 939–943.

Sato, S., and Harris, I. (1977). Superoxide dismutase from *Thermus aquaticus*. Eur. J. Biochem. *73*, 373–381.

Sato, S., and Nakasawa, K. (1978). Purification and properties of superoxide dismutase from *Thermus thermophilus HB8*. J. Biochem. (Tokyo) *83*, 1165–1171.

Smith, M. W., and Doolittle, R. F. (1992). A comparison of evolutionary rates of the two major kinds of superoxide dismutase. J. Mol. Evol. *34*, 175–184.

Stallings, W. C., Pattridge, K. A., Strong, R. K., and Ludwig, M. L. (1984). Manganese and iron superoxide dismutases are structural homologs. J. Biol. Chem. *259*, 10695–10699.

Stine, O. C., Dover, G. J., Zhu, D., and Smith, K. D. (1992). The evolution of two west African populations. J. Mol. Evol. *34*, 336–344.

Stoddard, B. L., Howell, P. L., Ringe, D., and Petsko, G. (1990a). The 2.1 Å resolution structure of iron superoxide dismutase from *Pseudomonas ovalis*. Biochemistry *29*, 8885–8893.

Stoddard, B. L., Ringe, D., and Petsko, G. A. (1990b). The structure of iron superoxide dismutase from *Pseudomonas ovalis* complexed with the inhibitor azide. Protein Eng. *4*, 113–119.

Tainer, J. A., Getzoff, E. D., Beem, K. M., Richardson, J. S., and Richardson, D. C. (1982). Determination and analysis of the 2 Å structure of copper, zinc superoxide dismutase. J. Mol. Biol. *160*, 181–217.

Tainer, J. A., Roberts, V. A., Fisher, C. L., Hallewell, R. A., and Getzoff, E. D. (1991). Mechanism and structure of superoxide dismutases. In A Study of Enzymes II. Mechanism of Enzyme Action, S. A. Kuby, ed. (Boca Raton, Florida: CRC Press), pp. 499–538.

Taylor, R. (1992). Mitochondrial DNA may hold a key to human degenerative diseases. J. NIH Res. *4*, 62–66.

Touati, D. (1988). Molecular genetics of superoxide dismutases. Free Radic. Biol. Med. *5*, 393–402.

Wagner, U. G., Werber, M. M., Beck, Y., Hartman, J. R., Frolow, F., and Sussman, J. L. (1989). Characterization of crystals of genetically engineered human manganese superoxide dismutase. J. Mol. Biol. *206*, 787–788.

Wallace, D. C. (1992). Diseases of the mitochondrial DNA. Annu. Rev. Biochem. *61*, 1175–1205.

White, C. W., Avraham, K. B., Shanley, P. F., and Groner, Y. (1991). Transgenic mice with expression of elevated levels of copper-zinc superoxide dismutase in the lungs are resistant to pulmonary oxygen toxicity. J. Clin. Invest. *87*, 2162–2168.

Wispe, J. R., Clark, J. C., Burhans, M. S., Kropp, K. E., Korfhagen, T. R., and Whitsett, J. A. (1989). Synthesis and processing of the precursor for human mangano-superoxide dismutase. Biochem. Biophys. Acta *994*, 30–36.

Wong, G. H. W., Elwell, J. H., Oberley, L. W., and Goeddel, D. V. (1989). Manganous superoxide dismutase is essential for cellular resistance to cytotoxicity of tumor necrosis factor. Cell *58*, 923–931.

Yoon, J. W. (1990). The role of viruses and environmental factors in the induction of diabetes. Curr. Top. Microbiol. Immunol. *164*, 95–123.

Zweier, J. L., Flaherty, J. T., and Weisfeldt, M. L. (1987). Direct measurement of free radical generation following reperfusion of ischemic myocardium. Proc. Natl. Acad. Sci. USA *84*, 1404–1407.